

A Four-Quadrant Modulation Technique to Extend Modulation Index Range for Multilevel Selective Harmonic Elimination/Compensation Using Staircase Waveforms

Hui Zhao, *Student Member, IEEE*, and Shuo Wang, *Senior Member, IEEE*

Abstract—One critical drawback of staircase multilevel selective harmonic elimination and compensation is that the modulation index range is very narrow. As a result, its application is limited. This paper presents a technique to transform the transcendental equations to geometry-based voltage phasor diagrams to explore the reason for the limited solution range and proposes a four-quadrant modulation technique to extend the modulation index range. Moreover, this paper investigates the inductor design considering both compensation capacity and undesired harmonic injection. Finally, the simulation and experimental results verify that the proposed modulation technique can greatly extend the modulation index range so it can be implemented in a wide range of applications.

Index Terms—Cascaded H-bridge (CHB), four-quadrant modulation, modulation index range, phasor diagram, selective harmonic elimination (SHE)/compensation, staircase multilevel inverter.

I. INTRODUCTION

MULTILEVEL converters/inverters, including neutral point clamped, flying capacitor, cascaded H-bridge (CHB), and modular multilevel converters/inverters, have drawn much attention in recent years, especially in medium and high voltage/power applications, such as motor drive systems, traction, PV inverters, and battery charging stations [1]–[3]. Their advantages include high reliability, low voltage stress, low electromagnetic interference (EMI), and low common-mode voltages. The optimal PWM modulation techniques, including selective harmonic elimination (SHE)/selective harmonic compensation (SHC) [4], [5] have been applied in multilevel converters [6]/inverters [4], [5], [7], [8] to achieve optimal performance with low switching frequency in various applications such as static synchronous compensator [4] and active power filters [5]. In these techniques, the transcendental equations to be solved are developed based on voltage/current references, THD

requirement, and other optimized objectives with the help of Fourier transformation. Step modulation [9] is one of the techniques employed in the SHE/SHC. For the step modulation, each switch in an H-bridge (HB) only switches ON and OFF once in every line period.

Techniques including iterative numerical algorithms [1], [10], online calculations [5], [6], [11], and the complete solution [12] have been proposed to solve the transcendental equations. However, it has been proved that the effective modulation index range of these techniques is very narrow. Therefore, their applications are very limited. To extend the modulation index range, [8] uses hybrid SHE and carrier-based sinusoidal PWM (SPWM) techniques. In this technique, when SHE modulation technique cannot find solutions within certain modulation index ranges, the SPWM technique is employed to find the solutions for the modulation index ranges. However, the switching frequency and the switching power loss will be increased with this technique. References [6] and [11] extend the modulation index range by greatly sacrificing the number of harmonics to be controlled. Because of this, with this technique, the current cannot fulfill the harmonic requirements. The techniques of using unequal dc-link voltages [13], [14] or nonsymmetrical modulation [15], [16] are employed to extend the modulation index range. However, all of these techniques greatly increase the complexity of the switching angle calculations. Moreover, the extended modulation index range is still very narrow. A practical technique with the full modulation index range was first proposed in [17] and [18]. The basic idea is to change the dc-link voltage of all HB from 0 to $1.2E$ (E is the nominal dc-link voltage) but keep their switching angles constant. Because the output voltage is proportional to the dc-link voltage, changing the dc-link voltage can change the modulation index. However, this technique needs extra dc/dc converters on the dc-link side. As a result, the hardware is complicated and switching power loss is increased. Moreover, when dc-link voltages are low, the switching angle of HB is very sensitive to the second-order harmonics on dc-link voltage; finally, $1.2E$ dc-link voltage adds 20% more voltage stress than the conventional techniques.

This paper proposes a voltage phasor diagram to transform the transcendental equations to geometry-based diagrams. Based on the diagram, it is found that the constraint of the switching angle range is the most critical factor limiting the

Manuscript received June 1, 2016; revised September 20, 2016; accepted October 14, 2016. Date of publication October 26, 2016; date of current version January 31, 2017. This work was supported by the National Science Foundation under Award 1540118. Recommended for publication by Associate Editor Hui Li. (*Corresponding author: Shuo Wang.*)

The authors are with the Power Electronics and Electrical Power Research Laboratory, University of Florida, Gainesville, FL 32611 USA (e-mail: shuo.wang@ece.ufl.edu).

This is a Special Issue on Electric Ship MVDC, 2016.

Color versions of one or more of the figures in this paper are available online at <http://ieeexplore.ieee.org>.

Digital Object Identifier 10.1109/JESTPE.2016.2622158

2168-6777 © 2016 IEEE. Personal use is permitted, but republication/redistribution requires IEEE permission. See http://www.ieee.org/publications_standards/publications/rights/index.html for more information.

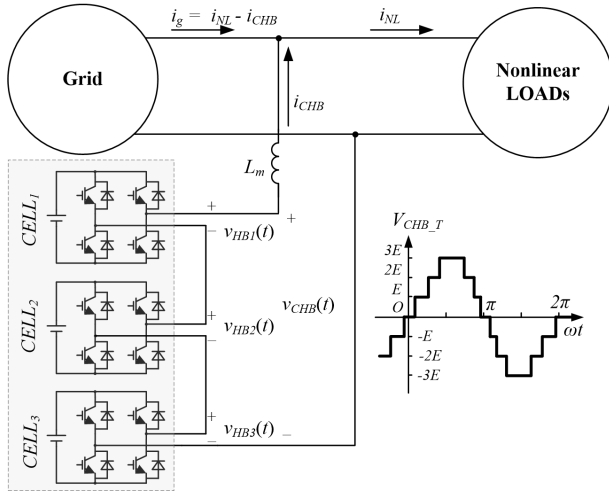


Fig. 1. Typical topology and waveforms of a three-cell CHB system.

modulation index range. Based on this finding, a four-quadrant modulation technique is proposed to significantly extend the modulation index range. A full modulation index range can be achieved with the proposed technique. This has been validated using numeration. Moreover, theoretical analysis and hardware implementation have been carried out in this paper.

In Fig. 1, a three-cell CHB is tied to a grid with nonlinear loads. The load current is i_{NL} , the grid current is i_g , and the current injected to the grid from the CHB is i_{CHB} . The output voltage of the CHB is v_{CHB} . The coupling inductor between the CHB and the grid has an inductance of L_m . It is well known that, with different modulation techniques, the inductor design is also different. This paper discusses the differences in the inductor design between SPWM and SHE/SHC. Based on SHE/SHC applications, the effects of inductance on both the compensation capacity and the attenuation of undesired harmonics are analyzed. Guidelines for the inductor design in multilevel SHE/SHC applications are proposed to ensure that the system complies with the harmonic standard.

This paper is organized as follows. Section II introduces the technique to transform the staircase multilevel voltage spectrum to a geometry-based voltage phasor diagram. Based on the phasor diagram, the reason for the limited modulation index range with conventional modulation techniques is explored. The critical factor limiting the modulation index range is identified. A four-quadrant modulation technique is proposed to significantly extend the modulation index range. Section III analyzes the effects of the inductor on the compensation capacity and the attenuation of undesired harmonics. The guidelines for inductor design are proposed. In Section IV, the simulation and experimental results validate the proposed four-quadrant modulation technique with a CHB topology.

II. FOUR-QUADRANT SWITCHING ANGLE MODULATION TECHNIQUE

A. Voltage Phasor Diagram and Four-Quadrant Switching Angle Modulation

In Fig. 1, half-wave symmetry modulation is used to compensate for the odd harmonics [4], [6] in a CHB topology.

For one HB, the output voltage $v_{HB}(t)$ can be expressed as

$$v_{HB}(t) = \begin{cases} E, & 2n\pi + \theta_r < \omega_g t < 2n\pi + \theta_f \\ -E, & (2n+1)\pi + \theta_r < \omega_g t < (2n+1)\pi + \theta_f \\ 0, & \text{otherwise} \end{cases} \quad (1)$$

where E is the dc bus voltage of an HB; ω_g is the fundamental angular frequency, which is 2π (60) rad/s in this paper; and θ_r and θ_f are the switching angles at rising and falling transitions of an HB.

The Fourier series for $v_{HB}(t)$ can be expressed as

$$v_{HB}(t) = \sum_{h=1}^{\infty} (a_{HB_h} \cos(h\omega t) + b_{HB_h} \sin(h\omega t)) \quad (2)$$

$$\begin{cases} a_{HB_h} = -\frac{2E}{\pi h} (\sin(h\theta_r) - \sin(h\theta_f)) \\ b_{HB_h} = \frac{2E}{\pi h} (\cos(h\theta_r) - \cos(h\theta_f)) \end{cases} \quad (3)$$

where h is the harmonic order and $h = 1, 3, 5, \dots$

The complex HB output voltage V_{HB_h} of the h th order harmonic is defined as $V_{HB_h} = a_{HB_h} + jb_{HB_h}$, then the magnitude of each order harmonic is $|V_{HB_h}|$, and the initial phase is $\angle V_{HB_h}$. The expression of V_{HB_h} can be rewritten as

$$V_{HB_h} = \frac{2E}{\pi h} ((-\sin(h\theta_r) + j \cos(h\theta_r)) - (-\sin(h\theta_f) + j \cos(h\theta_f))). \quad (4)$$

Based on Euler equation, $-\sin(h\theta) + j \cos(h\theta) = e^{j(h\theta + \pi/2)}$, (4) can be rewritten as

$$V_{HB_h} = \frac{2E}{\pi h} (e^{j(h\theta_r + \pi/2)} - e^{j(h\theta_f + \pi/2)}). \quad (5)$$

If the base voltage for the h th order harmonic is E/h , (5) can be rewritten in per unit

$$V_{HB_h}^p = \frac{2}{\pi} (e^{j(h\theta_r + \pi/2)} - e^{j(h\theta_f + \pi/2)}). \quad (6)$$

The voltage phasor diagrams can be developed based on (6). The voltage phasor $V_{HB_h}^p$ is determined by two vectors $(2/\pi)e^{j(h\theta_r + \pi/2)}$ and $(2/\pi)e^{j(h\theta_f + \pi/2)}$. As shown in Fig. 2, if $\theta_r \in [0, \pi/2]$ and $\theta_f \in [\pi/2, \pi]$ [1], [19], the ranges of phasors of $(2/\pi)e^{j(h\theta_r + \pi/2)}$ and $(2/\pi)e^{j(h\theta_f + \pi/2)}$ are the blue and red arcs, respectively, in Fig. 2(a)–(c) for $h = 1, 3, 5$. The green region represents the range of phasor V_{HB_h} , and it is derived by the ranges of the phasors $(2/\pi)e^{j(h\theta_r + \pi/2)}$ and $(2/\pi)e^{j(h\theta_f + \pi/2)}$. In Fig. 2(c), for the fifth-order harmonic, because both the ranges of $5\theta_r$ and $5\theta_f$ exceed 360° , the range of V_{HB_5} covers the whole area inside the range circle with an actual radius $4E/5\pi$. Similarly when $h > 5$, all the voltage phasors cover the whole range circles with the actual radius $4E/h\pi$ (they are not shown in Fig. 2). The actual amplitudes of the voltage phasors in Fig. 2 should be multiplied by E/h . As shown in Fig. 2(a), because switching angles θ_r and θ_f have limited ranges $[0, \pi/2]$ and $[\pi/2, \pi]$, the range of the synthesized fundamental voltage phasor V_{HB_1} is very limited, so it cannot cover the full modulation index range. The same rule can also be applied to the analysis of the synthesized third-order voltage harmonic V_{HB_3} . Extending the

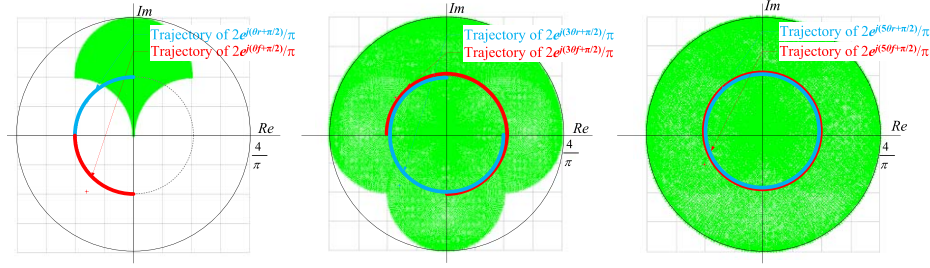


Fig. 2. Voltage phasor diagram (per unit) of one HB with $\theta_r \in [0, \pi/2]$ and $\theta_f \in [\pi/2, \pi]$. (a) Range of fundamental voltage $V_{HB_1}^D$. (b) Range of the third voltage $V_{HB_3}^D$. (c) Range of the fifth voltage $V_{HB_5}^D$.

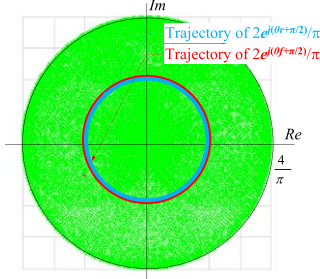


Fig. 3. Fundamental voltage phasor diagram (per unit) of one HB with $\theta_r \in [-\pi, \pi]$ and $\theta_f \in [-\pi, \pi]$.

range of θ_r and θ_f can therefore increase the ranges of the synthesized phasors and the modulation index range. Fig. 3 shows the range of the fundamental voltage phasor with θ_r and θ_f extended to $[-\pi, \pi]$. Because both the trajectories of $(2/\pi)e^{j(h\theta_r+(\pi/2))}$ and $(2/\pi)e^{j(h\theta_f+(\pi/2))}$ cover the full angle range, the synthesized voltage phasor V_{HB_1} covers the whole range circle with the actual radius $4E/\pi$. Because all the voltage harmonic phasors fully cover the range circles, they are not shown in this paper.

Figs. 2(c) and 3 show that if there are no limitations on the range of $h\theta_r$ and $h\theta_f$, two phasors $(2/\pi)e^{j(h\theta_r+(\pi/2))}$ and $(2/\pi)e^{j(h\theta_f+(\pi/2))}$ can synthesize any phasor within the circle with a radius equal to $4/\pi$. This conclusion can be proved by the algebraic method. If V_{REF_h} is defined as $V_{REF_h} = (4/\pi)R_{REF}e^{j\theta_{REF}}$, where $R_{REF} \leq 1$ is a nonnegative real number related to the magnitude of V_{REF_h} , and $\theta_{REF} \in [0, 2\pi]$ is the phase of V_{REF_h} . V_{REF_h} can represent any phasor inside the circle with a radius equal to $4/\pi$.

If $h\theta_r$ and $h\theta_f$ are

$$\begin{cases} \theta_M = \arccos(R_{REF}) \\ h\theta_r = (\theta_{REF} - \theta_M) - \frac{\pi}{2} \\ h\theta_f = (-\pi + \theta_{REF} + \theta_M) - \frac{\pi}{2} \end{cases}$$

the synthesized phasor $((2/\pi)e^{j(h\theta_r+(\pi/2))} - (2/\pi)e^{j(h\theta_f+(\pi/2))})$ is equal to V_{REF_h} as proved below

$$\begin{aligned} & \frac{2}{N\pi}e^{j(h\theta_r+\frac{\pi}{2})} - \frac{2}{N\pi}e^{j(h\theta_f+\frac{\pi}{2})} \\ &= \frac{2}{N\pi}(e^{j(\theta_{REQ}-\theta_M)} - e^{j(-\pi+\theta_{REQ}+\theta_M)}) \\ &= \frac{2}{N\pi}(e^{j(\theta_{REQ}-\theta_M)} - e^{-j\pi}e^{j(\theta_{REQ}+\theta_M)}) \end{aligned}$$

$$\begin{aligned} &= \frac{2}{N\pi}(e^{j(\theta_{REQ}-\theta_M)} + e^{j(\theta_{REQ}+\theta_M)}) \\ &= \frac{2}{N\pi}(\cos(\theta_{REF} - \theta_M) + j \sin(\theta_{REF} - \theta_M) \\ &\quad + \cos(\theta_{REF} + \theta_M) + j \sin(\theta_{REF} + \theta_M)) \\ &= \frac{2}{N\pi}(2 \cos(\theta_{REF}) \cos(\theta_M) + j 2 \sin(\theta_{REF}) \cos(\theta_M)) \\ &= \frac{4}{N\pi} \cos(\theta_M)(\cos(\theta_{REF}) + j \sin(\theta_{REF})). \end{aligned}$$

After θ_r and θ_f are extended to $[-\pi, \pi]$, compared with the conventional single quadrant switching angles within $[0, \pi/2]$ and $[\pi/2, \pi]$, the switching angles are four quadrants. The four-quadrant switching angles can synthesize a full modulation index while the single quadrant switching angles cannot.

To verify the proposed four-quadrants' switching angle modulation, the proposed modulation technique is applied to the three-cell, seven-level cascaded multilevel inverter in Fig. 1 with the SHE technique. The references of the third and fifth harmonics are set to zero, and the reference of the fundamental voltage changes from 0 to $3E$ with phase equal to zero degree. Optimized toolbox with generic algorithm in MATLAB is used to find the switching angle solutions [4], [10]. The objective function is set as $OF = |E_1| + |E_3| + |E_5|$, where E_h is the difference between the voltage reference and the actual CHB voltage resulted from the obtained solutions. Fig. 4(a) shows solution trajectories within full voltage modulation range from 0 to $3E$; Fig. 4(b) is the per unit difference for both the real and imaginary parts between the voltage references and the actual CHB voltage resulted from the obtained solutions. For the fundamental, the per unit differences of the real and imaginary parts of the fundamental voltage are defined as $E_{a_1} = \text{Re}(V_{CHB_1} - V_{Ref_1})/(NE)$, and $E_{b_1} = \text{Im}(V_{CHB_1} - V_{Ref_1})/(NE)$, where V_{CHB_1} is the actual fundamental output voltage of the CHB, V_{Ref_1} is the fundamental reference voltage and $N = 3$ is the number of cells. Because the harmonic voltage reference is zero, the per unit differences of harmonic voltages are defined as $E_{a_h} = \text{Re}(V_{CHB_h})/(NE/h)$, and $E_{b_h} = \text{Im}(V_{CHB_h})/(NE/h)$, where V_{CHB_h} is the actual harmonic output voltage of the CHB. From Fig. 4(a), the proposed four-quadrant modulation can find the solutions within the whole voltage range $[0, 3E]$ and the per-unit error is less than 5%. On the other hand, with the conventional single quadrant switching angle modulation technique, the modulation is only valid

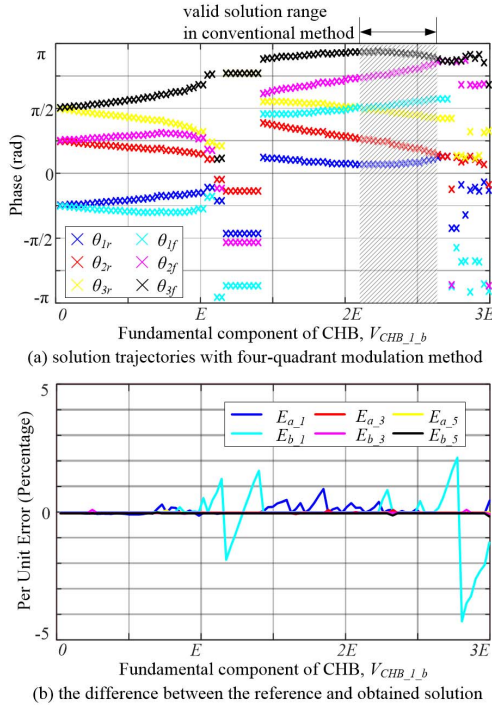


Fig. 4. Solution trajectories in a seven-level cascaded inverter with step modulation.

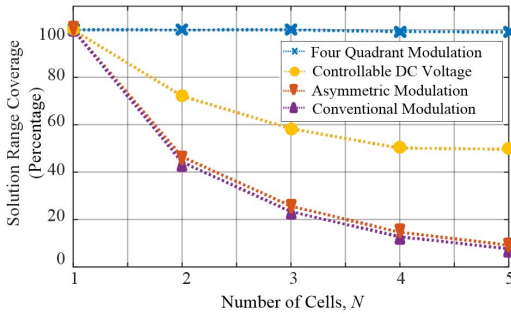


Fig. 5. Modulation index range versus number of cells with different modulation techniques.

for $[2.10E, 2.67E]$ (the shaded area). For this three-cell, seven-level cascaded multilevel inverter, the four-quadrant switching angle modulation technique can therefore expand the modulation index range by more than five times compared with the conventional technique.

A comparison between the proposed four-quadrants switching angle modulation and other conventional modulation techniques is shown in Fig. 5. Fig. 5 shows the relationship of the modulation index range in percentage, which is defined as $(\text{actual modulation index range})/(\text{full modulation index range})$ versus the number of HB cells of the CHB with different modulation techniques. Here, the *full modulation index range* is from 0 to NE . In Fig. 5, all the modulation techniques aim to eliminate the low order harmonics and control the amplitude of the fundamental component. For the variable dc modulation technique, the dc-link voltage of each HB can vary from $0.5E$ to E [13], [14], [16], [18]. Fig. 5 shows that the proposed four-quadrant switching angle modulation

technique can always achieve full modulation index range; while for other modulation techniques, increasing the number of HB cells greatly reduces the modulation index range.

B. Implementation of the Proposed Modulation Technique

In an HB, depending on the relationship between θ_r , θ_f , and the 0° , the number of the switching states equals $P_3^3 = 6$. All the possible switching states are shown in Fig. 6(a). In the implementation, a microcontroller is used to differentiate each switching state and generate the correspondent driving signals.

$|\theta_r - \theta_f| > \pi$ is not realizable with an HB, but theoretically, it could happen with four-quadrant switching angle modulation technique as the states 3s and 4s shown in Fig. 6(b). Since they cannot be realized using an HB, they are undesired states. To avoid these undesired switching states, $|\theta_r - \theta_f| < \pi$ can be used as a constraint in switching angle calculations, but this would complicate the calculations. This problem can be simply avoided by reassigning new switching angles θ'_r and θ'_f as in (7) for state 3s and (8) for state 4s

$$\begin{cases} \theta'_r = -\pi + \theta_f \\ \theta'_f = \pi + \theta_r \end{cases} \quad (7)$$

$$\begin{cases} \theta'_r = \pi + \theta_f \\ \theta'_f = -\pi + \theta_r. \end{cases} \quad (8)$$

In (7) for state 3s, the ranges of new switching angles are $\theta'_r \in [-\pi, 0]$ and $\theta'_f \in [0, \pi]$. Because $\theta'_f - \theta'_r = (\theta_r - \theta_f) + 2\pi \in [0, \pi]$, the new switching state will belong to state 3.

The new synthesized voltage phasor V'_{HB_h} with the reassigned switching angles is identical to the original V_{HB_h} . This can be proved in (9) because harmonic order h is odd and $e^{-jh\pi} = e^{jh\pi} = -1$

$$\begin{aligned} V'_{HB_h} &= \frac{2E}{\pi h} (e^{j(h\theta'_r + \frac{\pi}{2})} - e^{j(h\theta'_f + \frac{\pi}{2})}) \\ &= \frac{2E}{\pi h} (e^{j(h(-\pi + \theta_f) + \frac{\pi}{2})} - e^{j(h(\pi + \theta_r) + \frac{\pi}{2})}) \\ &= \frac{2E}{\pi h} (e^{-jh\pi} e^{j(h\theta_f + \frac{\pi}{2})} - e^{jh\pi} e^{j(h\theta_r + \frac{\pi}{2})}) \\ &= \frac{2E}{\pi h} (e^{j(h\theta_r + \frac{\pi}{2})} - e^{j(h\theta_f + \frac{\pi}{2})}) = V_{HB}(h). \end{aligned} \quad (9)$$

The similar analysis can be applied to state 4s. The ranges of new switching angles are $\theta'_r \in [0, \pi]$, and $\theta'_f \in [-\pi, 0]$. Because $(\theta'_r - \theta'_f) = (\theta_f - \theta_r) + 2\pi \in [0, \pi]$, the new switching state will belong to state 4.

The new synthesized phasor V'_{HB_h} is identical to the original V_{HB_h} , as proved in

$$\begin{aligned} V'_{HB_h} &= \frac{2E}{\pi h} (e^{j(h\theta'_r + \frac{\pi}{2})} - e^{j(h\theta'_f + \frac{\pi}{2})}) \\ &= \frac{2E}{\pi h} (e^{j(h\theta_r + \frac{\pi}{2})} - e^{j(h\theta_f + \frac{\pi}{2})}) = V_{HB}(h). \end{aligned} \quad (10)$$

The implementation of the proposed four-quadrant switching angle modulation for each HB is as shown in Fig. 7. There are three inputs: grid voltage $v_g(t)$, θ_r and θ_f , and the four driving signals: $g1$, $g2$, $g3$, and $g4$. Block 1 is the PLL block to obtain the phase information of $v_g(t)$; Block 2 is to detect states 3s and 4s and to convert them to state 3 and state 4

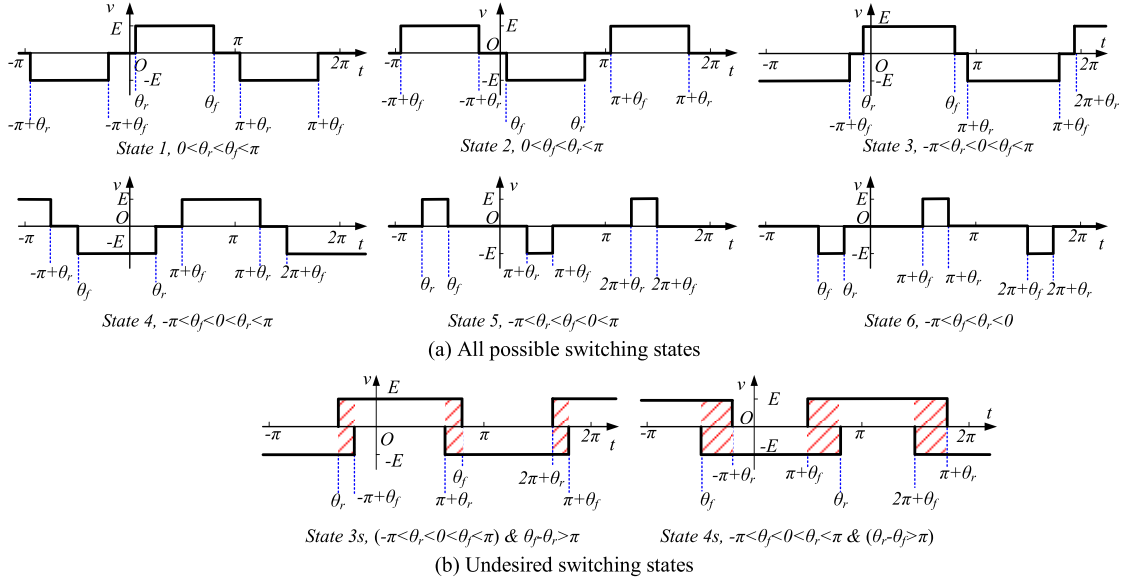


Fig. 6. All the possible switching cases with the proposed four-quadrant modulation. (a) All possible switching states. (b) Undesired switching states.

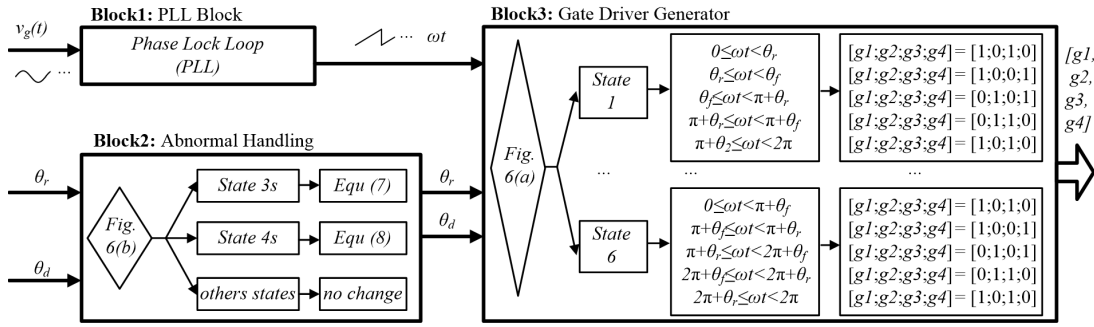


Fig. 7. Digital implementation of the four-quadrant switching angle modulation technique for each HB.

using (7) and (8) respectively; Block 3 uses the phase information and switching angles to generate the driving signals.

It should be pointed out that, in Fig. 6(a), different switching states may generate identical waveforms. For example, *states* 1 and 6, or *states* 2 and 5 can generate identical waveforms. This indicates that duplicated solutions exist in the proposed four-quadrant switching angle modulation technique. Because this does not have any negative impacts on the implementation or calculations, this paper does not discuss it in detail.

The proposed four-quadrant switching angle modulation technique can be applied to different grid applications such as harmonic elimination, harmonic mitigation, and harmonic compensation.

III. INDUCTOR DESIGN

In Fig. 1, inductor L_m 's design is critical because it has significant impact on the power density, compensation capacity, and current quality of the system. With the SPWM technique, large inductance can reduce the undesired switching harmonics injected to the power grid, but a large inductance decreases the compensation current capacity. Because of this, the upper and lower bounds of the inductance are calculated based on the

compensation capacity and the attenuation requirement for the switching harmonics, respectively. In multilevel SHE/SHC, the inductor design process is similar, but the values of the bounds are different from the SPWM technique.

This section first explores the inductor design constraint based on the fundamental component compensation. Second, the relationship between the inductance L_m and the injected CHB current harmonic spectrum envelope is analyzed. Third, based on the injected CHB current harmonic spectrum envelope, inductor design constraints for both the controllable harmonics, which are related to the compensation capacity, and uncontrollable harmonics, which are related to the attenuation of undesired harmonics, are discussed, respectively. Finally, an inductor design procedure is proposed based on all of these constraints.

This section will only discuss grid-tied SHC. The generalized solution can be applied to all grid-tied applications such as SHE and all offline applications.

A. Current Spectrum Envelope of a CHB

The output voltage of the CHB is the sum of all HB voltages, so the time domain waveform and frequency domain

spectrum can be expressed as

$$v_{\text{CHB}}(t) = \sum_{i=1}^N (v_{\text{HB}_i}(t)) \quad (11)$$

$$V_{\text{CHB}_h} = \sum_{i=1}^N (V_{\text{HB}_i_h})$$

$$= \frac{2NE}{\pi h} \sum_{i=1}^N (e^{j(h\theta_{if} + \frac{\pi}{2})} - e^{j(h\theta_{ir} + \frac{\pi}{2})})$$

$$h = 1, 3, \dots \quad (12)$$

where h is the order of specific HB and i is the sequence number of HBs, and θ_{ir} and θ_{if} are the switching angles at rising and falling transitions of the i th HB.

With the proposed four-quadrant switching angle modulation technique, the generated V_{CHB_h} can cover the full range circle with radius equal to $4NE/\pi h$

$$|V_{\text{CHB}_h}| \leq 4NE/(\pi h). \quad (13)$$

The output current of the CHB is

$$I_{\text{CHB}_h} = \begin{cases} \frac{V_{\text{CHB}_h} - V_g}{j\omega_g L}, & h = 1 \\ \frac{V_{\text{CHB}_h}}{jh\omega_g L}, & h = 3, 5, \dots \end{cases} \quad (14)$$

From (14) and (15), the spectrum envelope $|I_{\text{CHB}_h}|_{\text{ENV}}$ for harmonics ($h > 1$) is

$$|I_{\text{CHB}_h}|_{\text{ENV}} = \frac{|V_{\text{CHB}_h}|_{\text{max}}}{h\omega_g L} = \frac{4NE}{h^2\pi\omega_g L}, \quad h = 3, 5, \dots \quad (16)$$

where $|V_{\text{CHB}_h}|_{\text{max}}$ is the maximum magnitude of all the possible h th order harmonics.

The CHB's fundamental current will be discussed later.

B. Constraints on the Fundamental Component Compensation

For fundamental compensation, the following condition should be met:

$$V_{\text{CHB}_1} = j\omega_g L^* I_{\text{REF}_1} + V_g \quad (17)$$

where I_{REF_1} is the reference fundamental current for the CHB. I_{REF_1} can be active (for generator or battery charging function), reactive (for STATCOM function), or zero (for harmonic compensation function).

From (13) and (17), for the fundamental component, the following constraint for I_{REF_1} should be met: $|V_{\text{CHB}_1}| = |j\omega_g L^* I_{\text{REF}_1} + V_g| \leq 4NE/\pi$.

If $|V_{\text{CHB}_1}|_{\text{max}}$ can meet the condition defined above, the condition can always be satisfied for any I_{REF_1} . Because the fundamental reference current is $I_{\text{REF}_1} = |I_{\text{REF}_1}|_{\text{max}} \angle (\arg(V_g) - 90^\circ)$, $|V_{\text{CHB}_1}| = |V_{\text{CHB}_1}|_{\text{max}} = \omega_g L |I_{\text{REF}_1}|_{\text{max}} + |V_g| \leq 4NE/\pi$, and the constraint for L is therefore

$$\begin{cases} L_{\text{fun}} = \frac{4NE/\pi - |V_g|}{\omega_g |I_{\text{REF}_1}|_{\text{max}}} \\ L \leq L_{\text{fun}}. \end{cases} \quad (18)$$

C. Constraints on Harmonic Compensation Capacity

For convenience, the harmonics of a multilevel SHC are divided into controllable harmonics and uncontrollable harmonics. If the magnitude and phase of a harmonic can be controlled with the proposed four-quadrant switching angle modulation technique, it is controllable harmonic. Otherwise, it is uncontrollable harmonic. It is assumed that the proposed technique is used to control the low order harmonics so high order harmonics cannot be controlled due to limited number of switching angles. If H is the highest order of all the controllable harmonics, for $h < H$, I_{CHB_h} can always be controlled.

As shown in Fig. 1, if I_{NL_h} is the harmonic current generated from nonlinear load on the grid, for both the controllable and uncontrollable harmonics, the grid current I_{g_h} after compensation is given by (19), and its magnitude should meet the harmonic standards I_{STD_h} in (20)

$$I_{g_h} = I_{\text{NL}_h} - I_{\text{CHB}_h}, \quad h = 1, 3, 5, \dots \quad (19)$$

$$|I_{g_h}| < |I_{\text{STD}_h}|, \quad h = 3, 5, \dots \quad (20)$$

For the controllable harmonics, to guarantee the grid current harmonic as small as possible, the current references can be designed as in

$$\begin{cases} I_{\text{REF}_h} = I_{\text{NL}_h}, & \text{if } |I_{\text{CHB}_h}|_{\text{ENV}} \geq I_{\text{NL}_h} \\ I_{\text{REF}_h} = |I_{\text{CHB}_h}|_{\text{ENV}} \angle I_{\text{NL}_h}, & \text{if } |I_{\text{CHB}_h}|_{\text{ENV}} < I_{\text{NL}_h}. \end{cases} \quad (21)$$

In (21), if I_{CHB_h} can be higher than I_{NL_h} , the current reference for the h th order harmonic will be equal to I_{NL_h} , then a full compensation is achieved. If I_{CHB_h} cannot be higher than I_{NL_h} , the current reference would have the maximum magnitude (the envelop magnitude) and the same phase as I_{NL_h} . Then $|I_{g_h}| = |I_{\text{NL}_h} - I_{\text{CHB}_h}| = |I_{\text{NL}_h}| - |I_{\text{CHB}_h}|_{\text{ENV}}$. The L_m design should guarantee $|I_{\text{NL}_h}| - |I_{\text{CHB}_h}|_{\text{ENV}} \leq I_{\text{STD}_h}$ or $|I_{\text{CHB}_h}|_{\text{ENV}} \geq |I_{\text{NL}_h}| - |I_{\text{STD}_h}|$.

Because of this, the constraint for harmonic compensation capacity | is

$$\begin{cases} I_{\text{cap}_h} = |I_{\text{NL}_h}| - |I_{\text{STD}_h}| & \text{for } h = 3, 5, \dots H. \\ |I_{\text{CHB}_h}|_{\text{ENV}} \geq I_{\text{cap}_h} \end{cases} \quad (22)$$

D. Constraints on Undesired Harmonics

For undesired uncontrollable harmonics above order H , the worst case has to be considered.

From (19) and (20), the constraint can be described as

$$\begin{aligned} |I_{g_h}|_{\text{max}} &= |I_{\text{NL}_h} - I_{\text{CHB}_h}|_{\text{max}} \\ &= |I_{\text{NL}_h}|_{\text{max}} + |I_{\text{CHB}_h}|_{\text{max}} \leq |I_{\text{STD}_h}| \end{aligned}$$

or

$$\begin{cases} I_{\text{und}_h} = |I_{\text{NL}_h}| - |I_{\text{STD}_h}| & \text{for } h > H. \\ |I_{\text{CHB}_h}|_{\text{ENV}} \leq I_{\text{und}_h} \end{cases} \quad (23)$$

The constraint above for $|I_{\text{CHB}_h}|_{\text{max}}$ holds when $|I_{\text{STD}_h}|$ is larger than $|I_{\text{NL}_h}|$; otherwise, the $|I_{\text{CHB}_h}|_{\text{max}}$ should be as small as possible when other constraints in Sections III-B and III-C are met.

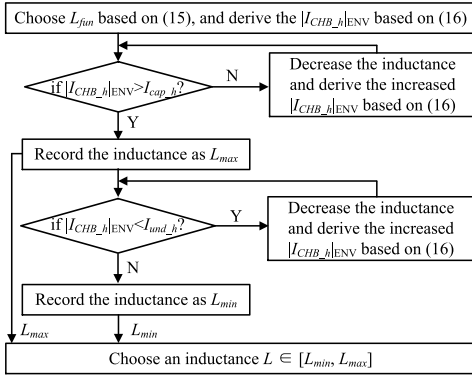


Fig. 8. Flowchart in Step 4 to determine the inductance range where the grid current after compensation can meet the constraints on fundamental compensation, harmonic compensation, and undesired harmonic injection.

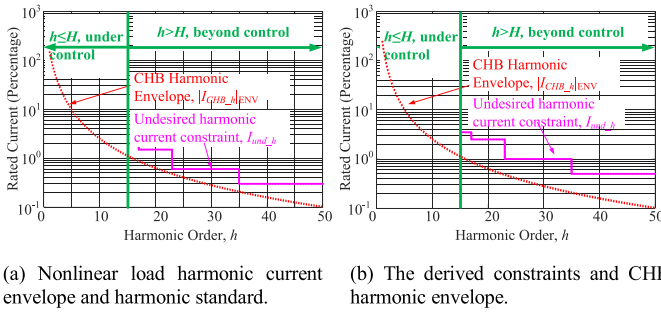


Fig. 9. Example of the proposed inductance design procedure. (a) Nonlinear load harmonic current envelope and harmonic standard. (b) Derived constraints and CHB harmonic envelope.

E. Procedure for Inductor Design

Based on the identified constraints above, the recommended inductor design procedure is as follows.

Step 1: Derive the limitation for L_{fun} based on the condition (18).

Step 2: Measure/calculate I_{NL_h} envelope and obtain harmonic current requirement I_{STD_h} from harmonic standard.

Step 3: Use (22) to derive the constraints on compensation capacity I_{cap_h} and use (23) to derive the constraints on undesired harmonic injection I_{und_h} .

Step 4: Decrease the inductance from L_{fun} , and find the range $[L_{min}, L_{max}]$ in which (15), (22), and (23) can be met at the same time. The detailed process is shown in Fig. 8. Finally, an inductance inside the range is selected.

Fig. 9 shows an example of the proposed inductor design procedure. In Step 1, condition (18) for L_{fun} is calculated. In Step 2, the current envelope of nonlinear load, I_{NL_h} , is calculated/measured and the harmonic requirement I_{STD_h} is obtained from the standard as shown in Fig. 9(a). In Step 3, the current constraints on compensation capacity I_{cap_h} are derived from (22) and plotted in blue in Fig. 9(b). The current constraints on undesired harmonic I_{und_h} are derived from (23) and plotted in magenta. In Step 4, an inductance L is determined and $|I_{CHB_h}|_{ENV}$ is derived based on (16) and is plotted in red. As shown in Fig. 9(b), because the red dotted line is above the blue constraints (i.e., $|I_{CHB_h}|_{ENV} > I_{cap_h}$) and

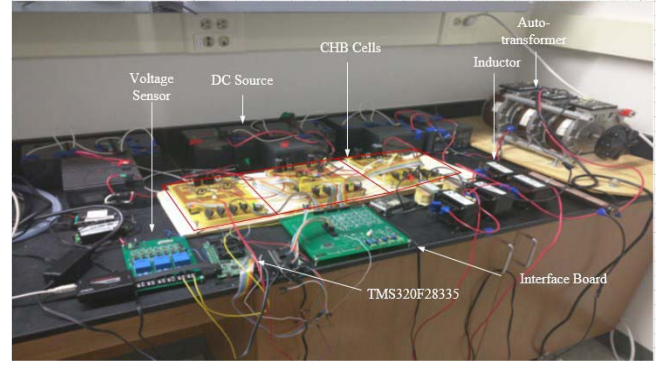


Fig. 10. (a)–(c) Topology of simulation and experiment. (d) Testbed prototype.

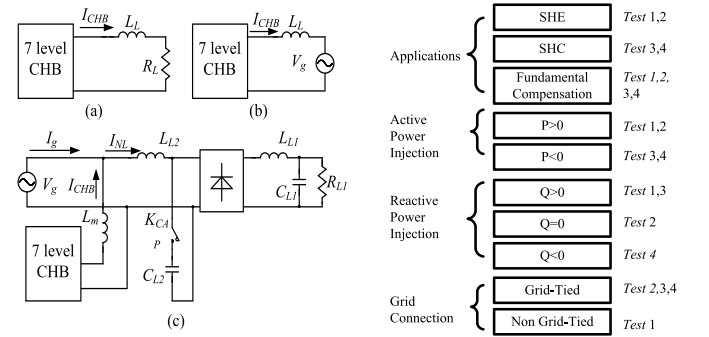


Fig. 11. Test plan.

TABLE I
CONFIGURATION OF THE SIMULATION AND EXPERIMENT

	Topology	Fundamental Parameters
Test 1	(a)	P=640W, Q=483VAR
Test 2	(b)	P=990W, Q=0
Test 3	(c), K_{CAP} OFF	P=-480W, Q=480 VAR
Test 4	(c), K_{CAP} ON	P=-390W, Q=-480 VAR

below the magenta constraints (i.e., $|I_{CHB_h}|_{ENV} < I_{cap_h}$), the constraints on both the compensation capacity and the undesired harmonics can be met.

IV. SIMULATION AND EXPERIMENT VERIFICATION

Simulation and experiment are conducted for a three-cell, 7 level 1 kVA prototype to validate the proposed four-quadrant switching angle modulation technique. It should be noted that the scale-down testbed is to validate the proposed modulation technique. The proposed modulation technique can be applied to any voltage levels, such as MVDC and HVDC, for multilevel SHE/SHC topologies to achieve a large modulation range. It should be pointed out that it is common to use scale-down testbed to validate modulation technique for high voltage/power systems [6], [7], [14], [19]. The circuit topology, test plan, and parameters are shown in Figs. 10 and 11, Tables. I and II, respectively. Simulations were conducted in MATLAB Simulink, and the experimental waveforms were recorded with Rigol MSO4054 digital oscilloscope.

TABLE II
PARAMETERS OF SIMULATION AND EXPERIMENT

Grid Voltage, V_g	110 V / 60 Hz
DC bus voltage, E	50 V
Number of cells, N	3
Inductance L_L	10 mH
Resistance R_L	5 ohm
Inductance L_{L1}	5 mH
Inductance L_{L2}	2.5 mH
Capacitance C_{L1}	1000 uF
Capacitance C_{L2}	400 uF
Inductance L_m	5 mH
Resistance R_{L1}	7.5 ohm (<i>Test 3</i>) 15 ohm (<i>Test 4</i>)

TABLE III
CALCULATED FOUR-QUADRANT SWITCHING ANGLES

	θ_r (deg)	θ_f (deg)	switching state
Test 1 $V_{CHB_1}^p=2.00$	112.4	106.8	State 2
	52.35	132.3	State 1
	12.16	166.8	State 1
Test 1* $V_{CHB_1}^p=2.00$ (conventional tech)	0	180	State 1
	55.76	90.93	State 1
Test 2 $V_{CHB_1}^p=2.80$	89.90	124.2	State 1
	-62.51	-143.0	State 6
	-22.96	177.5	State 3s
Test 3 $V_{CHB_1}^p=2.27$	-42.11	78.01	State 3
	31.10	162.8	State 1
	53.70	146.4	State 1
Test 4 $V_{CHB_1}^p=1.76$	88.67	105.5	State 1
	80.30	-174.9	State 4s
	-20.10	140.8	State 3
Test 5 $V_{CHB_1}^p=0.20$	42.31	30.25	State 2
	-50	-58	State 6
	87	58	State 2
Test 6 $V_{CHB_1}^p=1.00$	-87	130	State 6
	142	-131	State 4s
	24	38	State 1
	-24	131	State 3

The spectra from simulations and experiments were calculated using MATLAB FFT tool. The harmonic mitigation technique [18] was implemented, and up to the 15th harmonics can be controlled. A detailed inductor design based on the inductor design procedure is given in the Appendix. Harmonic standard IEEE 519 was used as the harmonic limitation. The calculated four-quadrant switching angles are shown in Table III.

Fig. 12 shows the experimental and simulation results for test 1 after applying the proposed four-quadrant switching angle modulation technique in the nongrid tied system with RL load in Fig. 9(a). With the four-quadrant switching angle modulation technique, the V_{CHB} is five-level instead of seven-level while the switching frequency is still 60 Hz in each HB. The current spectrum shows that the fundamental component, harmonic, and total demand distortion (TDD) meet the requirement.

If the conventional modulation technique is adopted, the switching angle solutions cannot be found. One practical solution is to sacrifice high order harmonics and only control fundamental and the third harmonics. The waveforms and the current spectra with a conventional single quadrant switching angle modulation technique are as shown in Fig. 13 for

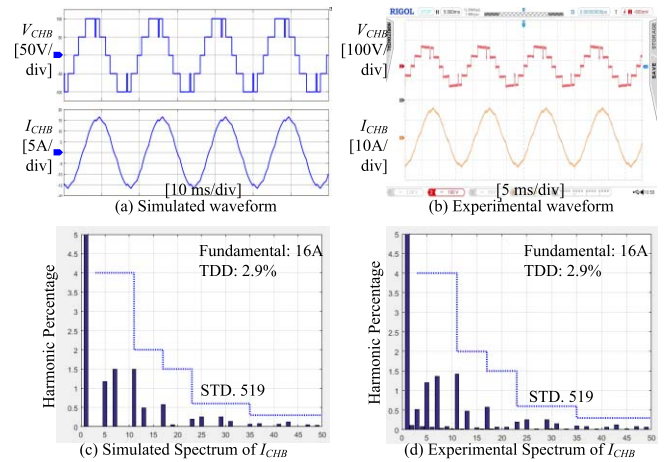


Fig. 12. Simulation and experimental results for test 1 using the proposed four-quadrant switching angle modulation technique.

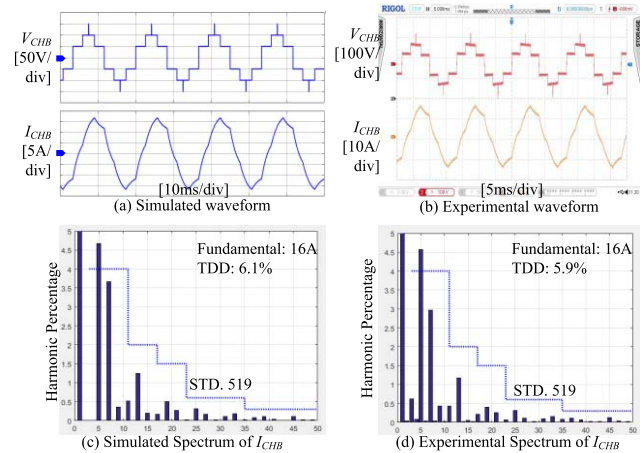


Fig. 13. Simulation and experimental results for test 1 using conventional modulation technique.

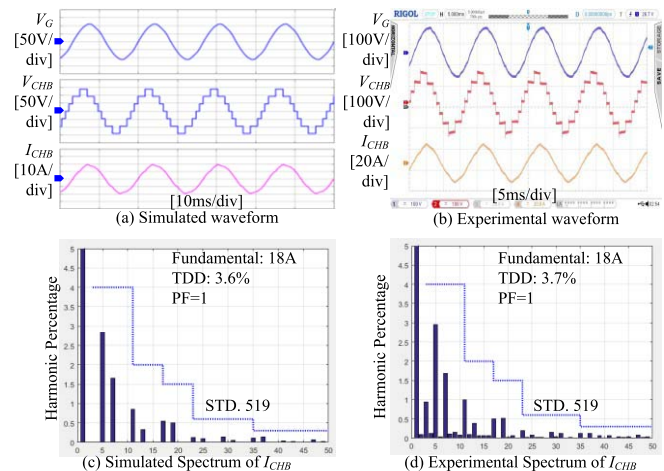


Fig. 14. Simulation and experimental results for test 2 using the proposed four-quadrant modulation technique.

test 1*. In the figure, the waveform is seven-level, but its current harmonic cannot meet the harmonic requirement. The comparison of Figs. 12 and 13 shows the advantages of the proposed modulation technique.

Fig. 14 shows the results of test 2 after the four-quadrant modulation is applied to a grid-tied CHB system. The results

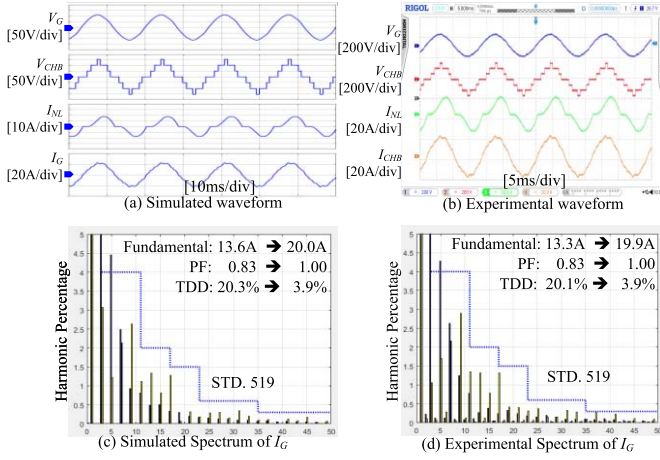


Fig. 15. Simulation and experimental results for *test 3* using the proposed four-quadrant modulation technique.

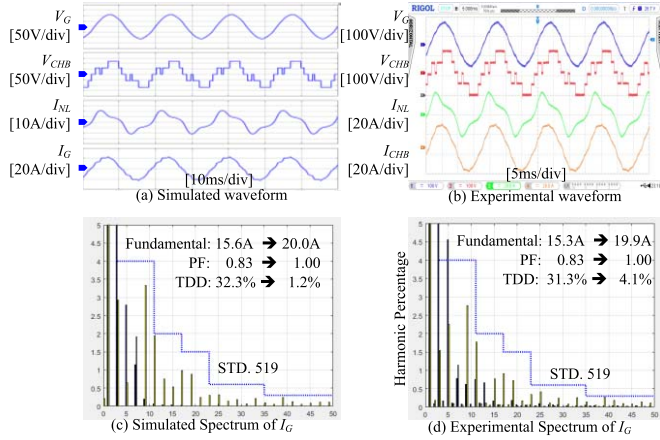


Fig. 16. Simulation and experimental results for *test 4* using the proposed four-quadrant modulation technique.

of test 3 in Fig. 15 and the results of test 4 in Fig. 16 show that the proposed four-quadrant modulation can be used to simultaneously draw active power from the grid to charge batteries, compensate the harmonics of nonlinear load, and compensate the reactive power on the grid. The harmonic spectra before and after compensations are shown in Figs. 15 and 16. The solid bars are the spectrum before the compensation and the empty bars are the spectrum after compensation. Both the simulation and experimental results show that the active power is well controlled as designed to charge batteries (i.e., PF was controlled to be unity), high order harmonics are below the standard, and TDD is below 5%.

From Figs. 12 to 18, six modulation indexes in $V_{CHB_1}^p = [0.2, 1, 1.76, 2, 2.27, 2.80]$ have been tested to demonstrate the effectiveness of the proposed four-quadrant modulation technique within a full modulation index range. The conventional single-quadrant switching angle modulation technique cannot find solutions for tests 1, 2, 4, 5, and 6, while the proposed four-quadrant modulation can find solutions without problems for all the tests. This proves that the proposed four-quadrant modulation technique can significantly extend the modulation index range.

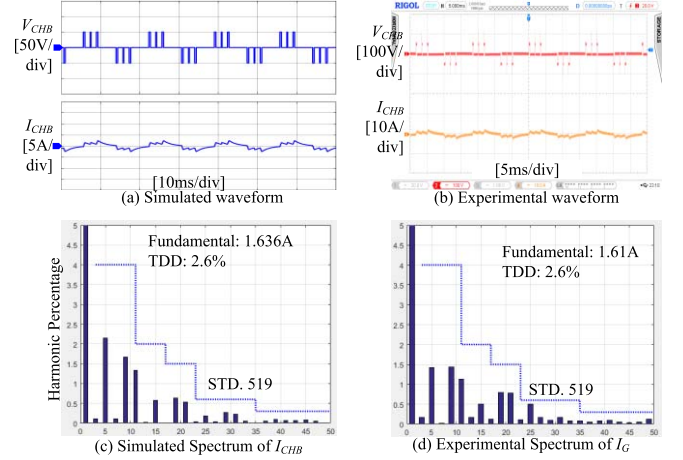


Fig. 17. Simulation and experimental results for *test 5* using the proposed four-quadrant modulation technique.

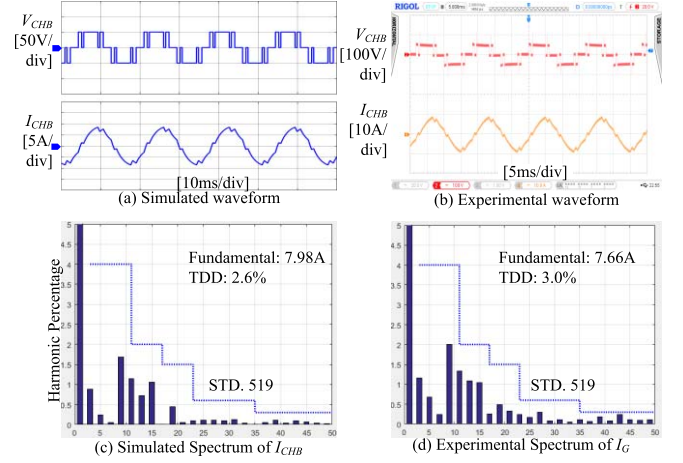


Fig. 18. Simulation and experimental results for *test 6* using the proposed four-quadrant modulation technique.

Figs. 17 and 18 show the simulation and experimental results in tests 5 and 6.

V. CONCLUSION

A four-quadrant switching angle modulation technique is proposed in this paper to significantly extend the modulation index range compared with the conventional modulation technique. Its implementation is discussed. The coupling inductor design based on fundamental component compensation constraint, harmonic compensation capacity constraint, and undesired current harmonic constraint is explored in detail. A design procedure is proposed. The simulation and experimental results verified that the proposed technique can be applied to various applications. The proposed modulation technique can be applied to any voltage/power levels to achieve a large modulation range.

APPENDIX

The Appendix shows the inductor design in Section IV.

Test 1 is an offline application. Therefore, $V_g = 0$, $Z = j\omega_g L + R$. (16) is transformed to $|I_{CHB_h}|_{ENV} = ((4E)/(h|Z|)) = ((4E)/(h((\omega_g L)^2 + R^2)^{1/2}))$, $h = 3, 5, 7$ and (18) is transformed to $Z_{fun} = ((4NE)/(\pi |I_{REF_1}|_{max}))$ and

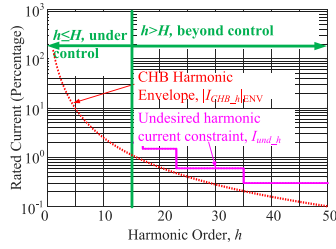


Fig. 19. Derived constraints and CHB harmonic envelope in test 1.

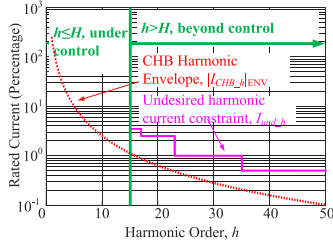


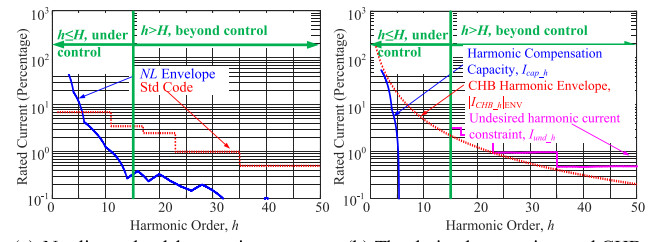
Fig. 20. Derived constraints and CHB harmonic envelope in test 2.

$L_{fun} = (Z_{fun}^2 - R^2)^{1/2} / \omega_g$. In Step 1, L_{fun} equals 21.6 mH. In Step 2, $I_{NL_h} = 0$ because no compensation is required in the system, and the current harmonic requirement I_{STD_h} is regulated by IEEE Std. 519 with its strictest limitation. In Step 3, from (22), $I_{cap_h} = -I_{STD_h} < 0$ indicates that no compensation requirement is required and from (23) $I_{und_h} = I_{STD_h}$. In Step 4, $L_{min} = 7.8$ mH and $L_{max} = 21.6$ mH. Therefore, a 10 mH inductor is used in the system. The relationship between the constraints and $|I_{CHB_h}|_{ENV}$ is shown in Fig. 19.

Test 2 is a grid-tied system with harmonic elimination. Similar to test 1, $I_{NL} = 0$ because there is no compensation requirement. The grid voltage is provided by a strong grid with an autotransformer, STACO 2513-3. In Step 1, $L_{fun} = 10.74$ mH. In Step 2, $I_{NL_h} = 0$ and the current harmonics are regulated by the limit I_{STD_h} defined in Std. 519. From (22), $I_{cap_h} = -I_{STD_h} < 0$ indicates that no compensation requirement is required and from (23) $I_{und_h} = I_{STD_h}$. In Step 4, $L_{min} = 4.6$ mH and $L_{max} = 10.74$ mH. A 10 mH inductor is used in the system. The relationship between the constraints and $|I_{CHB_h}|_{ENV}$ is shown in Fig. 20.

It should be noted that I_{STD_h} in Std. 519 is related to $|I_{SC}/I_{rated}|$, where I_{SC} is short current. Because Z_g is ignorable with a strong grid, and $Z_T = 0.32 + j0.078$, which is measured using an impedance analyzer, Keysight E4990A at 60 Hz, the short current is $I_{SC} = V_g / (Z_g + Z_T) = (459 - j112)$ A, and $|I_{SC}/I_{rated}| = 23.6$. The I_{STD_h} with grid-tied application is therefore different from that used in test 1 as compared in Figs. 19 and 20.

Tests 3 and 4 are for grid-tied systems that have the same working condition as in Section III. No extra equation transformation is needed. For test 3, in Step 1, $L_{fun} = 10.74$ mH and in Step 2, the I_{NL_h} and I_{STD_h} are shown in Fig. 21(a). In Step 3, I_{cap_h} and I_{und_h} are shown in Fig. 21(b). In Step 4, $L_{max} = 6.8$ mH and $L_{min} = 4.9$ mH. $L_m = 5$ mH is



(a) Nonlinear load harmonic current envelope and harmonic standard. (b) The derived constraints and CHB harmonic envelope.

Fig. 21. Inductor design procedure in test 3. (a) Nonlinear load harmonic current envelope and harmonic standard. (b) Derived constraints and CHB harmonic envelope.

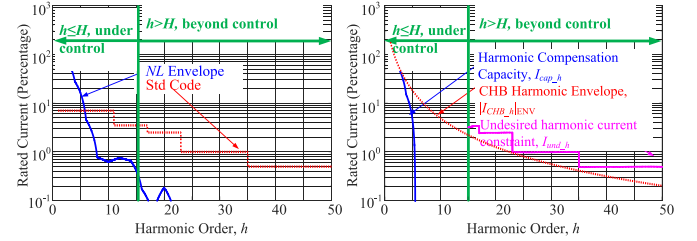


Fig. 22. Inductor design procedure in test 4. (a) Nonlinear load harmonic current envelope and harmonic standard. (b) Derived constraints and CHB harmonic envelope.

finally used in the system; $|I_{CHB_h}|_{ENV}$ is shown in Fig. 21(b). For test 4, $L_{fun} = 10.74$ mH, $L_{max} = 5.9$ mH, $L_{min} = 4.9$ mH, and $L_m = 5$ mH. The I_{NL_h} and I_{STD_h} are shown in Fig. 22(a). I_{cap_h} , I_{und_h} and $|I_{CHB_h}|_{ENV}$ are shown in Fig. 22(b).

It is important to note that the constraint for undesired current attenuation is calculated based on the worst scenario, which is rare in real applications. As a result, there is a large margin between the undesired harmonics and the standard. As shown in Figs. 14–18, although this paper designs inductors based on I_{STD_h} only with $|I_{SC}/I_{rated}| \in [20, 50]$, the actual current can meet the strictest requirement in Std. 519.

REFERENCES

- [1] M. S. A. Dahidah, G. Konstantinou, and V. G. Agelidis, "A review of multilevel selective harmonic elimination PWM: Formulations, solving algorithms, implementation and applications," *IEEE Trans. Power Electron.*, vol. 30, no. 8, pp. 4091–4106, Aug. 2015.
- [2] A. Marzoughi, R. Burgos, D. Boroyevich, and Y. Xue, "Investigation and comparison of cascaded H-bridge and modular multilevel converter topologies for medium-voltage drive application," in *Proc. 40th Annu. Conf. IEEE Ind. Electron. Soc. (IECON)*, Oct. 2014, pp. 1562–1568.
- [3] Y. Zhou and H. Li, "Analysis and suppression of leakage current in cascaded-multilevel-inverter-based PV systems," *IEEE Trans. Power Electron.*, vol. 29, no. 10, pp. 5265–5277, Oct. 2014.
- [4] Y. Chu, S. Wang, and R. Crosier, "Grid active power filters using cascaded multilevel inverters with direct asymmetric switching angle control for grid support functions," in *Proc. 28th Annu. IEEE Appl. Power Electron. Conf. Expo. (APEC)*, Mar. 2013, pp. 1332–1338.
- [5] H. Zhao and S. Wang, "A real-time selective harmonic compensation (SHC) based on asymmetric switching angle modulation and current feedback control for cascaded modular multilevel inverters," presented at the IEEE Appl. Power Electron. Conf. Expo. (APEC), Mar. 2015, pp. 2160–2166.
- [6] H. Zhao, T. Jin, S. Wang, and L. Sun, "A real-time selective harmonic elimination based on a transient-free inner closed-loop control for cascaded multilevel inverters," *IEEE Trans. Power Electron.*, vol. 31, no. 2, pp. 1000–1014, Feb. 2016.

- [7] H. Zhou, Y. W. Li, N. R. Zargari, G. Cheng, R. Ni, and Y. Zhang, "Selective harmonic compensation (SHC) PWM for grid-interfacing high-power converters," *IEEE Trans. Power Electron.*, vol. 29, no. 3, pp. 1118–1127, Mar. 2014.
- [8] A. Moeini, Z. Hui, and S. Wang, "High efficiency, hybrid selective harmonic elimination phase-shift PWM technique for cascaded H-bridge inverters to improve dynamic response and operate in complete normal modulation indices," in *Proc. IEEE Appl. Power Electron. Conf. Expo. (APEC)*, Mar. 2016, pp. 2019–2026.
- [9] Y. Liu, H. Hong, and A. Q. Huang, "Real-time calculation of switching angles minimizing THD for multilevel inverters with step modulation," *IEEE Trans. Ind. Electron.*, vol. 56, no. 2, pp. 285–293, Feb. 2009.
- [10] B. Ozpineci, L. M. Tolbert, and J. N. Chiasson, "Harmonic optimization of multilevel converters using genetic algorithms," *IEEE Power Electron. Lett.*, vol. 3, no. 3, pp. 92–95, Sep. 2005.
- [11] J. Wang and D. Ahmadi, "A precise and practical harmonic elimination method for multilevel inverters," *IEEE Trans. Ind. Appl.*, vol. 46, no. 2, pp. 857–865, Mar./Apr. 2010.
- [12] J. N. Chiasson, L. M. Tolbert, K. J. McKenzie, and Z. Du, "A complete solution to the harmonic elimination problem," *IEEE Trans. Power Electron.*, vol. 19, no. 2, pp. 491–499, Mar. 2004.
- [13] L. M. Tolbert, J. N. Chiasson, Z. Du, and K. J. McKenzie, "Elimination of harmonics in a multilevel converter with nonequal DC sources," *IEEE Trans. Ind. Appl.*, vol. 41, no. 1, pp. 75–82, Jan. 2005.
- [14] Y. Liu, H. Hong, and A. Q. Huang, "Real-time algorithm for minimizing THD in multilevel inverters with unequal or varying voltage steps under staircase modulation," *IEEE Trans. Ind. Electron.*, vol. 56, no. 6, pp. 2249–2258, Jun. 2009.
- [15] M. S. A. Dahidah, G. Konstantinou, N. Florentzou, and V. G. Agelidis, "On comparing the symmetrical and non-symmetrical selective harmonic elimination pulse-width modulation technique for two-level three-phase voltage source converters," *IET Power Electron.*, vol. 3, no. 6, pp. 829–842, Nov. 2010.
- [16] M. S. A. Dahidah and V. G. Agelidis, "Non-symmetrical SHE-PWM technique for five-level cascaded converter with non-equal DC sources," in *Proc. IEEE 2nd Int. Power Energy Conf. (PECon)*, Dec. 2008, pp. 775–780.
- [17] A. Moeini, H. Iman-Eini, and A. Marzoughi, "DC link voltage balancing approach for cascaded H-bridge active rectifier based on selective harmonic elimination-pulse width modulation," *IET Power Electron.*, vol. 8, no. 4, pp. 583–590, Apr. 2015.
- [18] M. Najjar, A. Moeini, M. K. Bakhshizadeh, F. Blaabjerg, and S. Farhangi, "Optimal selective harmonic mitigation technique on variable DC link cascaded H-bridge converter to meet power quality standards," *IEEE J. Emerg. Sel. Topics Power Electron.*, vol. 4, no. 3, pp. 1107–1116, Sep. 2016.
- [19] D. Hong, S. Bai, and S. M. Lukic, "Closed-form expressions for minimizing total harmonic distortion in three-phase multilevel converters," *IEEE Trans. Power Electron.*, vol. 29, no. 10, pp. 5229–5241, Oct. 2014.



Hui Zhao (S'14) received the bachelor's and master's degrees in electrical engineering from the Huazhong University of Science and Technology, Wuhan, China, in 2010 and 2013, respectively. He is currently pursuing the Ph.D. degree with the Electrical and Computer Engineering Department, University of Florida, Gainesville, FL, USA.

He was an Intern at the General Electric Global Research Center, Shanghai, China, in 2013. He has authored or co-authored several IEEE conference and transaction papers.



Shuo Wang (S'03–M'06–SM'07) received the Ph.D. degree from Virginia Tech, Blacksburg, VA, USA, in 2005.

From 2005 to 2009, he was a Research Assistant Professor at Virginia Tech. From 2009 to 2010, he was a Senior Design Engineer with GE Aviation Systems, Vandalia, OH, USA. From 2010 to 2014, he was with the University of Texas at San Antonio, San Antonio, TX, USA, first as an Assistant Professor and later as an Associate Professor. He has been an Associate Professor with the Department of Electrical and Computer Engineering, University of Florida, Gainesville, FL, USA, since 2015. He has authored more than 120 IEEE journal and conference papers and holds eight U.S. patents.

Dr. Wang was a recipient of the Best Transaction Paper Award from the IEEE Power Electronics Society in 2006 and two William M. Portnoy Awards for the papers published in the IEEE Industry Applications Society in 2004 and 2012, respectively. In 2012, he received the prestigious National Science Foundation CAREER Award. He is an Associate Editor of the IEEE TRANSACTIONS ON INDUSTRY APPLICATIONS and a Technical Program Co-Chair of the IEEE 2014 International Electric Vehicle Conference.